Electric field control of magnons in magnetic thin films: *Ab initio* predictions for two-dimensional metallic heterostructures

Alberto Marmodoro,[1,*] Sergiy Mankovsky,[2] Hubert Ebert,[2] Jan Minár,[3] and Ondřej Šipr[1,3]
[1]*FZU - Institute of Physics of the Czech Academy of Sciences, Cukrovarnická 10, CZ-162 53 Prague, Czech Republic*
[2]*Department of Chemistry, Ludwig-Maximilians-University Munich, Butenandtstrasse 11, D-81377 Munich, Germany*
[3]*New Technologies Research Centre, University of West Bohemia, CZ-301 00 Pilsen, Czech Republic*

(Received 15 February 2022; accepted 2 May 2022; published 12 May 2022)

We explore possibilities for control of magnons in two-dimensional heterostructures by an external electric field acting across a dielectric barrier. By performing *ab initio* calculations for a Fe monolayer and Fe bilayer, both suspended in vacuum and deposited on Cu(001), we demonstrate that external electric field can significantly modify magnon lifetimes and that these changes can be related to field-induced changes in layer-resolved Bloch spectral functions. For systems with more magnon dispersion branches, the gap between high- and low-energy eigenmodes varies with the external field. These effects are strongly influenced by the substrate. Considerable variability in how the magnon spectra are sensitive to the external electric field can be expected, depending on the substrate and on the thickness of the magnetic layer.

DOI: 10.1103/PhysRevB.105.174411

I. INTRODUCTION

Magnonics, i.e., the generation, control, and detection of collective spin excitations (or magnons) has been considered for possible information storage and processing applications due to the promise of higher data density and its more energy-efficient elaboration [1–6]. This area is rapidly advancing, from early proposals of memory devices to more recent examples concerning the implementation of logical operations [7–9].

Various groups have studied how an external electric field can be used to modify features of the magnon spectra and to potentially realize these functionalities. An early example has been the measurement of proportionality between magnetic resonance shifts and an applied electric field in lithium ferrite [10]. This observation has been explained as a consequence of a voltage-controlled magnetocrystalline anisotropy variation, and deemed small for practical applications [11]. Subsequently, multiferroic materials have been found to offer a stronger response in their magnon spectrum through the coupling between their intrinsic electric polarization and the externally applied perturbation [12,13]. More recently, Liu and Vignale discussed yet a different theoretical mechanism not restricted to this class of materials and capable to produce effective Dzyaloshinskii-Moriya interactions (DMI) proportional to the external field [14]. This has prompted to examine the consequences for magnon spectra [15–19], most frequently adopting as reference material the ferrimagnetic insulator yttrium iron garnet (YIG).

In this paper, we are interested in the possible control of magnons by an applied electric field acting, across a dielectric barrier, on a two-dimensional (2D) heterostructure. We deal with the idealized layout of magnetic/nonmagnetic layers of simple transition metals, e.g., Fe and Cu. Similarly to the case of YIG, absence of electric current due to the insulating barrier precludes energy dissipation into Joule heating (Ohmic losses). The gating E_{field} acts by controlling the hybridization between electronic states. We study how this can offer another venue for controlled variation of the magnon dispersion relation and lifetime. This latter aspect complements previous theoretical studies such as Refs. [20,21], which have typically examined only the adiabatic or infinitely long-lived limit of collective spin excitations.

This paper is structured as follows. We first describe a reference device layout and introduce the theoretical scheme adopted to study from *first principles* its magnon spectrum (Sec. II). We then present numerical results for an Fe monolayer and an Fe bilayer either suspended in vacuum or deposited on a Cu substrate. We show how the magnon lifetime and the gap between low- and high-energy eigenmodes depend on the external electric field and how this can be traced back to changes of the underlying electronic structure (Sec. III). We summarize salient aspects of the results in Sec. IV and offer our conclusions in Sec. V.

II. COMPUTATIONAL STRATEGY

We consider a metallic 2D heterostructure which contains a thin magnetic region on top of a nonmagnetic substrate and which is furthermore capped by a dielectric layer. A steady voltage between the substrate and an electrode located atop the dielectric barrier sets up a constant electric field E_{field} (Fig. 1). For the sake of clarity and simplicity, we model the dielectric barrier by a spacing vacuum gap, and we choose, respectively, Fe and Cu as the material of the magnetic and nonmagnetic layers.

*marmodoro@fzu.cz

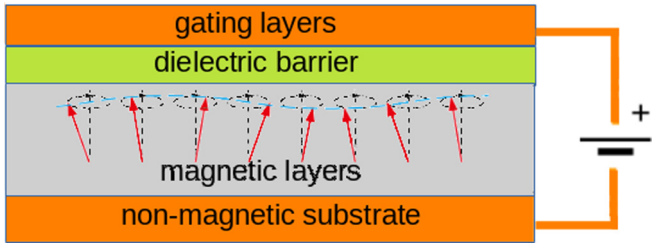

FIG. 1. Schematic device layout. Precessing magnetic moments (red arrows) that compose a magnon mode (blue wave) are studied as a function of an external electric field acting along the stacking direction across a dielectric barrier (green region) which prevents charge transport.

Our interest lies in how the applied voltage can control the spectrum of transverse spin-wave excitations or magnons. The magnons are confined within the magnetic layers because of the negligible proximity-induced spin polarization in copper. However, their dispersion relation $\omega_n(\boldsymbol{q})$, with $\boldsymbol{q}$ being the wave vector confined to the 2D Brillouin zone Ω_{BZ} and n labeling distinct eigenmodes, as well as their lifetime, depend significantly on the underlying substrate already in the absence of any applied $\mathrm{E}_{\mathrm{field}}$.

Various dissipation mechanisms can be responsible for a finite lifetime of magnons that manifests itself through the $\boldsymbol{q}$-dependent broadening of the above dispersion relation $\omega_n(\boldsymbol{q})$. Here we consider a 2D periodic, perfectly long-range ordered scenario in the zero temperature limit and we neglect therefore Bloch damping from disorder [22,23]. We also neglect dissipation through magnon-magnon scattering [24–26]. On the other hand, we consider Landau damping, which is due to the competition between magnons and single-particle Stoner spin-flip excitations with same energy and momentum, and which is deemed to be a dominant attenuation mechanism for magnons propagation in transition metals [27].

A. General approximation strategy

In the limit of sufficient timescale separation between fast electrons and slow precession of atomic magnetic moments, we can adopt as a starting point the Heisenberg Hamiltonian

$$H = -\sum_{i\neq j} J_{ij}\hat{\boldsymbol{e}}_i \cdot \hat{\boldsymbol{e}}_j, \tag{1}$$

where $\hat{\boldsymbol{e}}_i$ is the direction of magnetic moment around atom at position $\boldsymbol{R}_i$ [28]. The exchange coupling parameters J_{ij} can be calculated at a *first principles* electronic structure level by employing, for instance, the magnetic force theorem [29,30].

Extensions of the basic scheme [31,32] can be used to obtain the full tensor form, $J_{ij}^{\mu\nu}$ with $\mu(\nu) = x, y, z$, which can be of particular relevance in connection with relativistic effects such as spin-orbit coupling. Considering, for instance, ferromagnetic order along z, one can then identify the isotropic exchange interactions of Eq. (1) with $J_{ij} = \frac{1}{2}(J_{ij}^{xx} + J_{ij}^{yy})$, and can analogously define a DMI vector $\boldsymbol{D}_{ij} = (D_{ij}^x, D_{ij}^y, D_{ij}^z)$ with components $D_{ij}^x = \frac{1}{2}(J_{ij}^{yz} - J_{ij}^{zy})$, $D_{ij}^y = \frac{1}{2}(J_{ij}^{xz} - J_{ij}^{zx})$ and $D_{ij}^z = \frac{1}{2}(J_{ij}^{xy} - J_{ij}^{yx})$. Liu and Vignale [14] discussed how an applied electric field can produce an additional DMI term $H_{\mathrm{DM}} = \boldsymbol{D}_{ij} \cdot (\boldsymbol{S}_i \times \boldsymbol{S}_j)$, proportional to the perturbation and to the spin-orbit coupling strength.

Although reduced dimensionality can have a significant impact on spin-orbit coupling, magnetism in thin films is known to heavily depend on the interplay between substrate and magnetic layers already at the level of isotropic exchange interactions J_{ij}. Our goal is to explore to what extent the layout of Fig. 1 could be used to control magnon spectral features by exploiting field-dependent hybridization of electronic states, without depending on more subtle relativistic effects. We remain, therefore, within the description of Eq. (1), and we neglect other features such as magnetocrystalline anisotropy or Gilbert damping [31,33–35].

The precession of atomic magnetic moments around their ground-state direction in the effective magnetic field generated by all their neighbors, $\boldsymbol{B}_i^{\mathrm{eff}} = \sum_{j\neq i} J_{ij}\hat{\boldsymbol{e}}_j$, follows the Landau-Lifschitz equation of motion and can be studied as a secular equation problem. In particular, the adiabatic magnon spectrum is given by the eigenvalues of the lattice Fourier-transformed expression [20,28]

$$\widehat{N}(\boldsymbol{q})|\omega_n(\boldsymbol{q})\rangle = \omega_n(\boldsymbol{q})|\omega_n(\boldsymbol{q})\rangle, \tag{2}$$

with explicit matrix elements $[\underline{N}(\boldsymbol{q})]_{s,s'} = \langle s|\widehat{N}(\boldsymbol{q})|s'\rangle$. The subscript $s = 1, \ldots, N_{\mathrm{sub}}$ labels the (magnetic) sublattices with origin $\boldsymbol{b}_s$. Each atom therefore lies at position $\boldsymbol{R}_i = \boldsymbol{R}_I + \boldsymbol{b}_s$, where $\boldsymbol{R}_I$ is a vector of the periodic lattice. For a long-range ordered ground state with atomic magnetic moments $\boldsymbol{m}_s = (0, 0, m_s^z)$ the matrix $\underline{N}(\boldsymbol{q})$ has elements [36–39]

$$[\underline{N}(\boldsymbol{q})]_{s,s'} = \frac{4}{m_s^z}[J_{ss'}(\boldsymbol{0}) - J_{ss'}(\boldsymbol{q})]. \tag{3}$$

The Fourier transformation in Eq. (2) is performed over all displacements $\boldsymbol{R}_{IJ} = \boldsymbol{R}_I - \boldsymbol{R}_J$ between unit cells I and J:

$$J_{ss'}(\boldsymbol{0}) = \delta_{s,s'}\sum_{\boldsymbol{R}_{IJ}}\sum_{s''=1}^{N_{\mathrm{sub}}} J_{IsJs''},$$
$$J_{ss'}(\boldsymbol{q}) = \sum_{\boldsymbol{R}_{IJ}} J_{IsJs'}\, e^{-i\boldsymbol{q}\cdot(\boldsymbol{R}_{IJ}+\boldsymbol{b}_s-\boldsymbol{b}_{s'})}. \tag{4}$$

The above approach toward studying magnon spectra is intuitive, computationally expedite, and typically offers good agreement with experiment. However, it does not account for Landau damping. Physically, it originates from competition of collective transverse spin-wave excitations with single-particle spin-flip excitations [40–42]. A comprehensive scheme to account for both collective and single-particle magnetic excitations is provided by linear response formalism in the framework of the time-dependent density functional theory (TDDFT). This approach focuses on the dynamic transverse susceptibility $\underline{\chi}^{+(-)}(\boldsymbol{q}, \omega)$ which describes the response of spin-polarized electrons to a magnetic field precessing clockwise $(+)$ or anticlockwise $(-)$ with the frequency ω. This susceptibility is determined by the Dyson-like equation

$$\underline{\chi}^{+(-)}(\boldsymbol{q}, \omega) = [\underline{1} - \mathring{\underline{\chi}}^{+(-)}(\boldsymbol{q}, \omega)\underline{f}_{\mathrm{xc}}(\boldsymbol{q})]^{-1}\,\mathring{\underline{\chi}}^{+(-)}(\boldsymbol{q}, \omega), \tag{5}$$

where the kernel $\underline{f}_{\mathrm{xc}}(\boldsymbol{q})$ is the second derivative of the exchange-correlation energy with respect to local magnetic

moment [43,44] and $\underline{\mathring{\chi}}^{+(-)}(\boldsymbol{q},\omega)$ is the transverse susceptibility of noninteracting electrons. This quantity can be given at the scalar-relativistic level in terms of Kohn-Sham eigenstates ϕ_ν and eigenvalues ϵ_ν solving the spin-polarized Schrödinger problem. Simplifying for a moment the notation through restriction to the $N_{\rm sub}=1$ case, we have [41]

$$\mathring{\chi}^{+(-)}(\boldsymbol{r},\boldsymbol{r}',\boldsymbol{q},\omega)=\lim_{\eta\to 0^+}\sum_{\nu,\nu'}\int_{\Omega_{\rm BZ}}d\boldsymbol{k}\frac{\phi_\nu^{\uparrow(\downarrow),*}(\boldsymbol{k},\boldsymbol{r})\phi_{\nu'}^{\downarrow(\uparrow)}(\boldsymbol{k}+\boldsymbol{q},\boldsymbol{r})\phi_{\nu'}^{\downarrow(\uparrow),*}(\boldsymbol{k}+\boldsymbol{q},\boldsymbol{r}')\phi_\nu^{\uparrow(\downarrow)}(\boldsymbol{k},\boldsymbol{r}')}{\omega+i\eta+\epsilon_\nu^{\uparrow(\downarrow)}(\boldsymbol{k})-\epsilon_{\nu'}^{\downarrow(\uparrow)}(\boldsymbol{k}+\boldsymbol{q})}$$
$$\times\{\theta[E_F-\epsilon_\nu^{\uparrow(\downarrow)}(\boldsymbol{k})]-\theta[E_F-\epsilon_{\nu'}^{\downarrow(\uparrow)}(\boldsymbol{k}+\boldsymbol{q})]\},\tag{6}$$

with the Heaviside step function $\theta(x)=1$ for $x>0$, $\theta(x)=0$ for $x\leqslant 0$. The left (right) arrow selects the spin polarization relevant for the clockwise (anticlockwise) precession of the moments in response to the infinitesimal perturbation of the rotating magnetic field. The wave vectors for $\boldsymbol{k}$, $\boldsymbol{k}+\boldsymbol{q}$ are considered within the Brillouin zone $\Omega_{\rm BZ}$, and the positions $\boldsymbol{r}$, $\boldsymbol{r}'$ are restricted to the Wigner-Seitz cells around sites $\boldsymbol{R}_I$, $\boldsymbol{R}_J$, respectively. The quantities in Eqs. (5) and (6) can be cast in matrix form by adopting, e.g., a combined basis set of spherical harmonics and orthogonal polynomials to represent the $\boldsymbol{r}$, $\boldsymbol{r}'$ dependence [44,45].

Thanks to the fluctuation-dissipation theorem [46], the propensity of a material to host a magnetic excitation with wave vector $\boldsymbol{q}$ and energy ω is marked by large values in the loss matrix $\mathrm{Im}\underline{\chi}^{+(-)}(\boldsymbol{q},\omega)$. Technically, this is due to zeros from the first term, $\underline{1}-\underline{\mathring{\chi}}^{+(-)}(\boldsymbol{q},\omega)\underline{f}_{\rm xc}(\boldsymbol{q})$, as well as to singularities from the second term, $\underline{\mathring{\chi}}^{+(-)}(\boldsymbol{q},\omega)$, in Eq. (5). The outcome can be studied by examining the eigenvalues of $\mathrm{Im}\underline{\chi}^{+(-)}(\boldsymbol{q},\omega)$ as a function of $\boldsymbol{q}$ and ω [44,47].

Long-living collective excitations (magnons) are characterized by the occurrence, at each energy and wave vector, of as many sharply defined eigenvalues as the number of magnetic sublattices in the unit cell [44]. By following the sequence of such peaks, one can reconstruct their dispersion relation and compare it, for instance, with the simpler $\omega_n(\boldsymbol{q})$ outcome from Eq. (2).

Landau damping instead manifests itself through the emergence of multiple, no longer well-separated eigenvalues which lead, in practice, to a broadened magnon dispersion. The broadening can be interpreted as inversely proportional to a finite magnon lifetime due to competition with Stoner single-particle excitations. These spin-flip transitions are described, in particular, by the noninteracting susceptibility $\mathring{\chi}^{+(-)}(\boldsymbol{r},\boldsymbol{r}',\boldsymbol{q},\omega)$ [44] and are entirely neglected in the secular equation problem of Eq. (2).

To approximately account for this aspect of the magnon physics, we apply here at a *first principles* level an approximative procedure that has been proposed, among others, by Yosida [40] for simplified theoretical models, and adopted, e.g., by Kirschner *et al.* [48–50] for the interpretation of spin-polarized electron energy loss experiments in metallic thin films.

The procedure consists of two steps. First, we obtain the adiabatic dispersion relation $\omega_n(\boldsymbol{q})$ from Eq. (2). This involves diagonalizing for each $\boldsymbol{q}$ the real $N_{\rm sub}\times N_{\rm sub}$ matrix defined in Eq. (3). Such a procedure is much simpler than dealing with complex matrices of Eqs. (5) and (6), which need to be dealt with not only for each $\boldsymbol{q}$ but also for every trial energy ω and which are also much bigger, depending on the sampling in $\boldsymbol{r}$ and $\boldsymbol{r}'$.

Subsequently, the intensity of single-particle excitations $S_n^{+(-)}(\boldsymbol{q})$ is obtained by considering only Stoner spin-flip transitions between occupied and unoccupied Kohn-Sham states, such that their difference in energy and momentum corresponds to the magnon eigenmode under consideration $|\omega_n(\boldsymbol{q})\rangle$. The number of relevant transitions is estimated by convoluting the spin-polarized electronic Bloch spectral functions $A^{\uparrow(\downarrow)}(\boldsymbol{k},s,E)=-\frac{1}{\pi}\Im\, G^{\uparrow(\downarrow)}(\boldsymbol{k},s,E)$ where the electronic Green's function $G^{\uparrow(\downarrow)}(\boldsymbol{k},s,E)$ is the Lehmann resummation of Kohn-Sham eigenstates and eigenvalues already appearing in Eq. (6). In practice, we adopt the Korringa-Kohn-Rostoker (KKR) construction to directly obtain these Green's functions [51], calculate the Heisenberg exchange parameters J_{ij} [30] and solve the secular equation problem of Eq. (2), and then we evaluate the expression

$$S_n^{+(-)}(\boldsymbol{q})=\int_{E_{\rm min}}^{E_{\rm max}}dE\int_{\Omega_{\rm BZ}}d^3k\sum_{s=1}^{N_{\rm sub}}A^{\uparrow(\downarrow)}(\boldsymbol{k},s,E)\,\theta(E_F-E)\,A^{\downarrow(\uparrow)}(\boldsymbol{k}+\boldsymbol{q},s,E+\omega_n(\boldsymbol{q}))\,\theta(E+\omega_n(\boldsymbol{q})-E_F)$$
$$\times\sqrt{\mathrm{Re}[v_{n,s}(\boldsymbol{q})]^2+\mathrm{Im}[v_{n,s}(\boldsymbol{q})]^2},\tag{7}$$

where the double integration samples the full Brillouin zone $\Omega_{\rm BZ}$ and the energy interval $\mathrm{E}_{\rm min}=E_F-\max[\omega_n(\boldsymbol{q})]$, $\mathrm{E}_{\rm max}=E_F+\max[\omega_n(\boldsymbol{q})]$ around the Fermi level E_F. Occupied and unoccupied states are selected via the Heaviside step function, similarly to Eq. (6). Finally, the last term in Eq. (7) is the sublattice-projected magnitude of the complex-valued eigenvector $|\omega_n(\boldsymbol{q})\rangle:=(v_{n,1}(\boldsymbol{q}),v_{n,2}(\boldsymbol{q}),\ldots,v_{n,N_{\rm sub}}(\boldsymbol{q}))^\dagger$ from Eq. (2). In general, this quantity describes how the n magnon mode involves deviations from the ground state at each magnetic sublattice [28]. In this context, it is used to perform a weighted sum of Stoner spin-flip transitions which also originate from that sublattice and which are assumed to compete

proportionally more with the specific magnon mode, depending on how it involves the same atoms.

Compared to Eq. (6), the energy and momentum convolution of Eq. (7) only involves real quantities. We use the result to produce a magnon spectral function which includes the finite lifetime

$$A_{\mathrm{mag}}(\boldsymbol{q}, n, \omega) = -\lim_{\eta\to 0^+} \frac{|\omega_n(\boldsymbol{q})\rangle\,\langle\omega_n(\boldsymbol{q})|}{\omega + \mathrm{i}[\eta + S_n^{+(-)}(\boldsymbol{q})] - \omega_n(\boldsymbol{q})}. \tag{8}$$

We note that the approach is not as robust as the more rigorous but demanding formulation in terms of the loss matrix $\mathrm{Im}\underline{\chi}^{+(-)}(\boldsymbol{q}, \omega)$ from Eq. (5). Among various simplifications behind it, we deem as most severe the separate evaluation of the adiabatic dispersion $\omega_n(\boldsymbol{q})$ and of the broadening function $S_n^{+(-)}(\boldsymbol{q})$. These quantities are used within Eq. (8) to approximate complex magnon poles which would, in an exact treatment, follow from analyzing the dynamic transverse susceptibility.

The TDDFT Eq. (5) construction of the magnon spectral function evaluates collective and single-particle spin-flip excitations on equal footing, meaning that their relative spectral weights gets redistributed, depending for instance on the location of the wave vector $\boldsymbol{q}$ within the Brillouin zone, but it remains on the whole conserved. The approximated construction of Eq. (8) reproduces some of the same features, but does not guarantee conservation of the total spectral weight [44,52]. Numerical nevertheless tests provide good agreement with the trends obtained, e.g., in Ref. [53] using TDDFT, in particular, for the dispersion $\omega(\boldsymbol{q})$ and the Stoner intensity $S(\boldsymbol{q})$.

In this paper, our aim is not to obtain absolute values for the Landau damping but rather to investigate its relative changes as a function of the externally applied electric field efficiently. As long as the inaccuracies of the more expedited but less robust approach depend only weakly on this perturbation, we can expect reasonable trends for the ratio between lifetime estimated with $\mathrm{E}_{\mathrm{field}} = 0$ and $\mathrm{E}_{\mathrm{field}} \neq 0$.

B. Finite electric field and other technical aspects

The results discussed in the following have been produced using the *ab initio* spin-polarized multiple-scattering or KKR Green's function formalism [51] as implemented in the SPRKKR code [54]. The self-consistent field (SCF) ground state for the 2D heterostructure of Fig. 1 was obtained by solving the DFT problem in fully relativistic mode, relying on the local spin density approximation with the Vosko, Wilk, and Nusair parametrization for the exchange and correlation term [55]. This provides good agreement with magnetic spectroscopy experiments in metallic ultrathin magnets [20], when atomic positions are fixed as in this paper.

To deal with systems with only 2D periodicity, we used the tight-binding or screened KKR method [56]. Fe monolayers and bilayers suspended in vacuum were modeled by slabs consisting of one or two Fe layers embedded in vacuum represented by four layers of empty sites at each site. Fe monolayers or bilayers deposited on Cu(001) were treated as truly semi-infinite systems: the electronic structure was reconverged within the topmost 11 or 10 substrate layers, while at the bottom of this interaction zone the electronic structure was matched to the bulk. For the geometry, we used the experimental unit cell parameters of bulk copper for the substrate and the case of iron layers suspended in vacuum to better highlight the role of the heterogeneous stacking by changing only one aspect of the system at the time [57]. The axis of magnetization was assumed along the [001] direction, in agreement with calculations of the magnetocrystalline anisotropy energy (MAE) and other literature [58,59]. Although neglected in the magnon dispersion of Eq. (3) due to its tiny magnitude, this nonzero anisotropy suppresses instabilities of long-range ferromagnetic order for the 2D-periodic magnetic layer(s). We refer to, e.g., Ref. [20] for a more extensive review of magnon spectroscopy in similar ultrathin metallic systems.

The external electric field is introduced similarly as in Refs. [60,61], namely, by considering above the Fe layers an auxiliary array of point charges, separated from the surface by vacuum, during calculation of the SCF solutions and all other quantities. For sufficient areal density and vertical separation, this layer generates an electric field which can be considered constant [62,63], with intensity

$$E_{\mathrm{field}} = \frac{Q_{\mathrm{aux}}}{2\epsilon_0 A}, \tag{9}$$

where Q_{aux} is the point charge within the perturbation limits discussed, e.g., in Ref. [63] (positive for a field oriented antiparallel to the surface normal $\hat{z}$) per area of the 2D unit cell A, and ϵ_0 is the vacuum permitivity. For the multipole expansion of the Green function, the angular momentum cutoff $\ell_{\mathrm{max}} = 3$ was used. The energy integrals to obtain the SCF-DFT solutions, as well as the isotropic Heisenberg exchange interactions from the magnetic force theorem [30], were evaluated by contour integration on a semicircular path within the complex energy plane using 32 Gaussian-Legendre abscissae. The Brillouin zone integrals used an equispaced mesh with 16 000 $\boldsymbol{k}$ points or more over the whole Ω_{BZ}. The Stoner expression Eq. (7) was evaluated by sampling energy points parallel and near to the real axis.

For the ferromagnetic ground states studied in Sec. III, we only need to consider one chirality, meaning that we restrict ourselves to the (+) variant of Eqs. (5)–(7) [40,42,44].

III. RESULTS

We discuss here results for a Fe monolayer and a Fe bilayer, both suspended in vacuum as well as deposited on Cu(001) surface.

A. Fe monolayer and Fe bilayer in vacuum

We begin examining how the external electric field influences the spin-polarized density of states (DOS). Results for a Fe monolayer are shown in Fig. 2, with no visible effects. Magnon spectra appear similarly robust with respect to the perturbation and are therefore not shown.

If a second iron sheet is added, changes in the layer-resolved DOS start to appear but they are still very small. Therefore, to highlight the influence of the external perturbation $\mathrm{E}_{\mathrm{field}}$, we consider the difference between the DOS projected on individual layers,

$$\Delta n^{\uparrow(\downarrow)}(E) = n_{\mathrm{Fe}_1}^{\uparrow(\downarrow)}(E) - n_{\mathrm{Fe}_2}^{\uparrow(\downarrow)}(E).$$

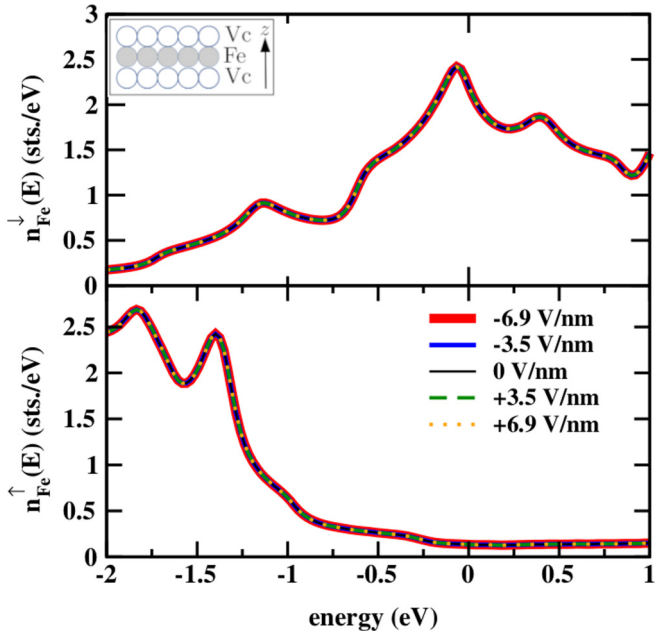

FIG. 2. DOS of a Fe monolayer suspended in vacuum for different values of E_{field}. All the curves fall essentially on top of each other, with no discernible effects from the electric field.

The outcome is shown in Fig. 3. If there is no external field, this difference is obviously zero because the bilayer is symmetric. With a finite E_{field}, the symmetry is removed and small energy- and spin-dependent transfer of electronic states between both layers occurs. This transfer is more pronounced for the minority states. Swapping the polarity of the perturbation, or the labeling of Fe_1 and Fe_2 layers, is equivalent to the $z \to -z$ coordinate transformation and leads to identical results. This will only change in the presence of a substrate which lifts the symmetry, as discussed in Sec. III B below.

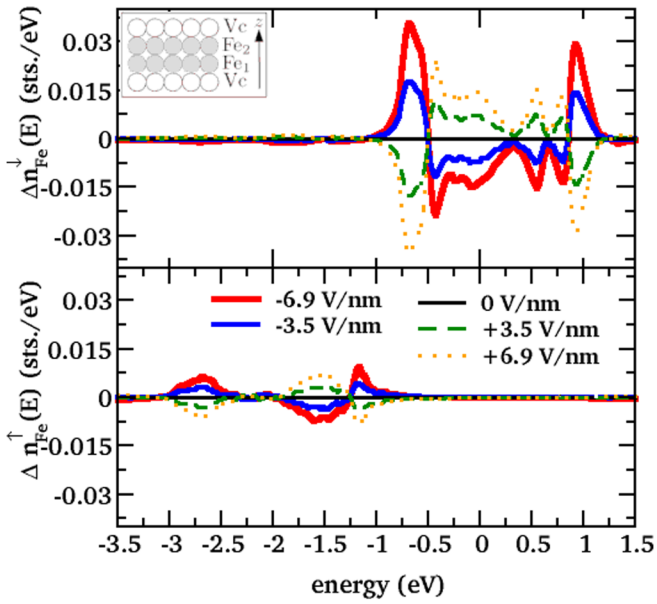

FIG. 3. Difference between the DOS projected on individual layers of a Fe bilayer as a function of E_{field}.

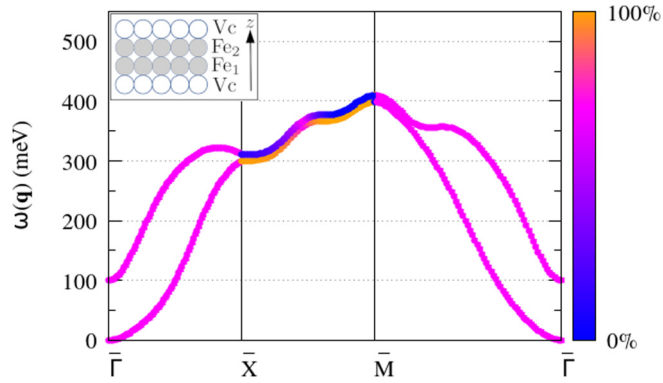

FIG. 4. Adiabatic magnon spectrum for the Fe bilayer suspended in vacuum with $E_{field} = 0$. The $\omega_2(\boldsymbol{q})$ solution is plotted with an artificial offset of +10 meV to allow visualization where energy degenerate. The color coding represents the magnitude of the corresponding complex eigenvectors, projected on the Fe_2 layer.

With only two magnetic layers, the secular equation problem expressed by Eqs. (2) and (3) reduces to diagonalizing the matrix

$$\underline{N}(\boldsymbol{q}) = 4\sum_{\boldsymbol{R}_{IJ}} \begin{pmatrix} \frac{J^{11}_{IJ}+J^{12}_{IJ}-J^{11}_{IJ}e^{-i\boldsymbol{q}\cdot\boldsymbol{R}_{IJ}}}{m_1^z} & \frac{-J^{12}_{IJ}e^{-i\boldsymbol{q}\cdot(\boldsymbol{R}_{IJ}+\boldsymbol{b}_1-\boldsymbol{b}_2)}}{m_1^z} \\ \frac{-J^{21}_{IJ}e^{-i\boldsymbol{q}\cdot(\boldsymbol{R}_{IJ}+\boldsymbol{b}_2-\boldsymbol{b}_1)}}{m_2^z} & \frac{J^{21}_{IJ}+J^{22}_{IJ}-J^{22}_{IJ}e^{-i\boldsymbol{q}\cdot\boldsymbol{R}_{IJ}}}{m_2^z} \end{pmatrix}, \quad (10)$$

having neglected here the much smaller contributions from the MAE. Results are shown in Fig. 4. We observe that eigenvalues are distinct between the $\overline{\Gamma}$ and the $\overline{X}$ point and between the $\overline{M}$ and the $\overline{\Gamma}$ point, i.e., when going from the center of the 2D Brillouin zone to its corners. For these portions of the spectrum, magnetic precession involves atoms from both layers. On the contrary, along the $\overline{X}$–$\overline{M}$ segment, i.e., at the Brillouin zone edge, eigenvalues are degenerate but precession involves exclusively one or the other iron sheet.

The effect of the external electric field on the magnon spectra is again very weak for this suspended Fe bilayer, so it would be hardly visible in a plot. Therefore, we focus just on the gap between the high- and low-energy branches at the $\overline{\Gamma}$ point (see Fig. 4). This gap can be evaluated as

$$\Delta E = \omega_2(\overline{\Gamma}) - \omega_1(\overline{\Gamma}) = 4\sum_{\boldsymbol{R}_{IJ}} J^{12}_{IJ}\,\frac{m_1^z + m_2^z}{m_1^z\, m_2^z}.$$

The dependence of this gap on E_{field} is shown in Fig. 5. We observe a very small variation for the considered range of E_{field}, just about 0.05%. Similarly as for Fig. 3, the graph in Fig. 5 is symmetric with respect to the polarity of the external field, in accordance with the interchangeable role of layer 1 and layer 2 in the absence of a substrate.

B. Fe monolayer on Cu(001) substrate

Larger effects can be expected for supported iron sheets because here the asymmetry introduced by the external field couples with the asymmetry stemming from the substrate. Figure 6 shows how the spin-polarized Fe-projected DOS varies with E_{field} for a Fe monolayer on Cu(001). The changes are now clearly visible, contrary to the situation for layers suspended in vacuum investigated in Figs. 2 and 3.

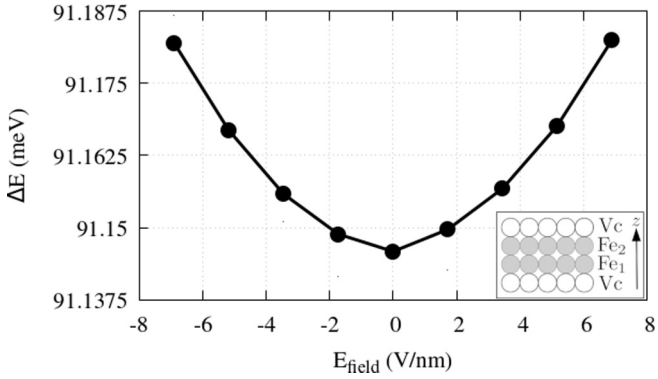

FIG. 5. Energy gap between the high- and low-energy magnon branches at $\boldsymbol{q} = \overline{\Gamma}$ for an iron bilayer suspended in vacuum (cf. Fig. 4) evaluated as a function of E_{field}.

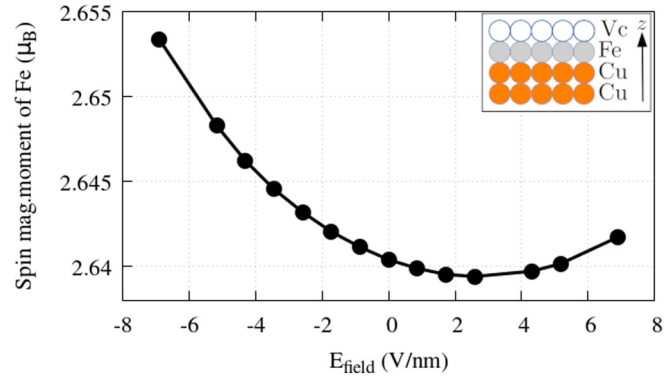

FIG. 7. Dependence of the magnetic moments at Fe sites on the external electric field for a Fe monolayer on Cu(001).

The corresponding change of the magnetic moment with E_{field} is shown in Fig. 7. The presence of the substrate means that the polarity of the external electric field matters this time—unlike in the case of suspended layers, as evidenced, e.g., in Fig. 5. Overall, the variation in the magnetic moment is quite small, about 0.5%.

A more detailed view can be obtained by inspecting the projection of the Bloch spectral function at the Fe site. Its dependence on E_{field} is outlined in Fig. 8. We show an interval around the Fermi level, which corresponds to the $\max[\omega_n(\boldsymbol{q})] = 0.5$ eV energy range of magnons in iron thin films.

Note that the Bloch spectral function exhibits the characteristic broadening from lack of periodicity along the z direction. Even though the general look of all three graphs is the same in Fig. 8, a systematic dependence of the position of certain features on E_{field} is evident: for example, the energy positions of the local maximum within 0.3 eV below E_F for $\boldsymbol{k}$ between $\overline{\Gamma}$ and $\overline{X}$ or the energy positions of the inflection point within 0.3 eV below E_F for $\boldsymbol{k}$ between $\overline{M}$ and $\overline{\Gamma}$.

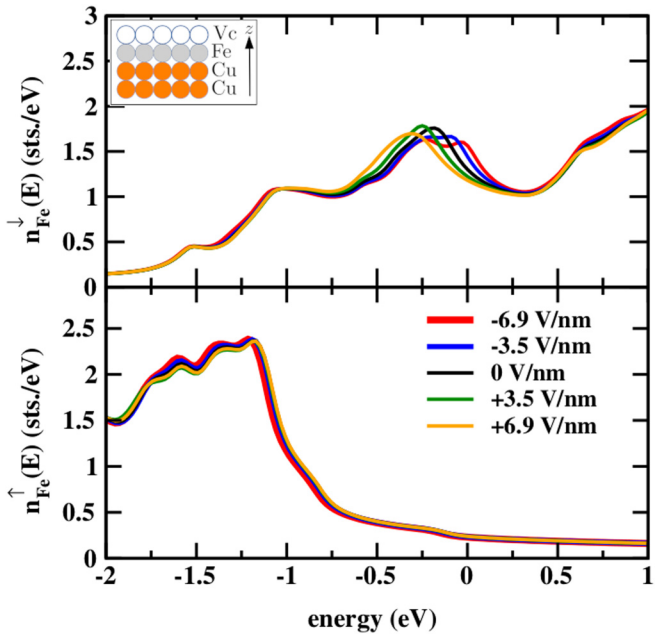

FIG. 6. Spin-polarized Fe-projected DOS for a Fe monolayer on Cu(001) for different intensities and polarities of the external electric field.

We show in Fig. 9 the dispersion relation $\omega(\boldsymbol{q})$ obtained according to Eq. (2) for the same three values of E_{field} considered in Fig. 8. We observe a very limited dependence. However, the situation is different for the Stoner spectrum estimated by means of Eq. (7). Results for $E_{field} = 0$ are first illustrated in the top graph of Fig. 10 as a broadening of the dispersion $\omega(\boldsymbol{q})$. The qualitative outcome of increasing Landau damping as we move away from the $\overline{\Gamma}$ point compares well both with experiments and with more comprehensive TDDFT [44] or model Hamiltonian RPA-based [64] calculations of the susceptibility. We interpret this broadening as inversely proportional to the magnon lifetime. The bottom graph of Fig. 10 shows the relative change of this quantity with E_{field}. Results are depicted for three choices of the $\boldsymbol{q}$ vector, indicated by dashed lines in the top graph of the same figure. It is evident that varying E_{field} leads to significant changes in the Stoner spectrum and, consequently, to different magnon lifetime. The general trend is that a positive E_{field} decreases the Landau damping thereby extending the magnon lifetime, whereas a negative E_{field} increases the damping and therefore reduces the magnon lifetime. The effect of a negative E_{field}, generated by having negative point charges above the Fe/Cu(001) semi-infinite system, appears to be larger than the effect of a positive E_{field}.

C. Fe bilayer on Cu(001)

In Sec. III B, we investigated a system with a single magnon eigenmode. To have more eigenmodes, it is necessary to consider more than a single Fe sheet. The Cu substrate has only a negligible induced magnetic moment and thus cannot host magnons. We consider in this section an iron bilayer on Cu(001), again assuming out-of-plane easy axis of magnetization and the same unrelaxed lattice parameters as in the previous sections, to facilitate comparison.

We first examine the dependence of the magnetic moments in both Fe layers on E_{field}. For the upper Fe_2 layer, exposed to the vacuum, this dependence has got a similar nonmonotonous profile as for the iron monolayer on Cu(001) (compare the

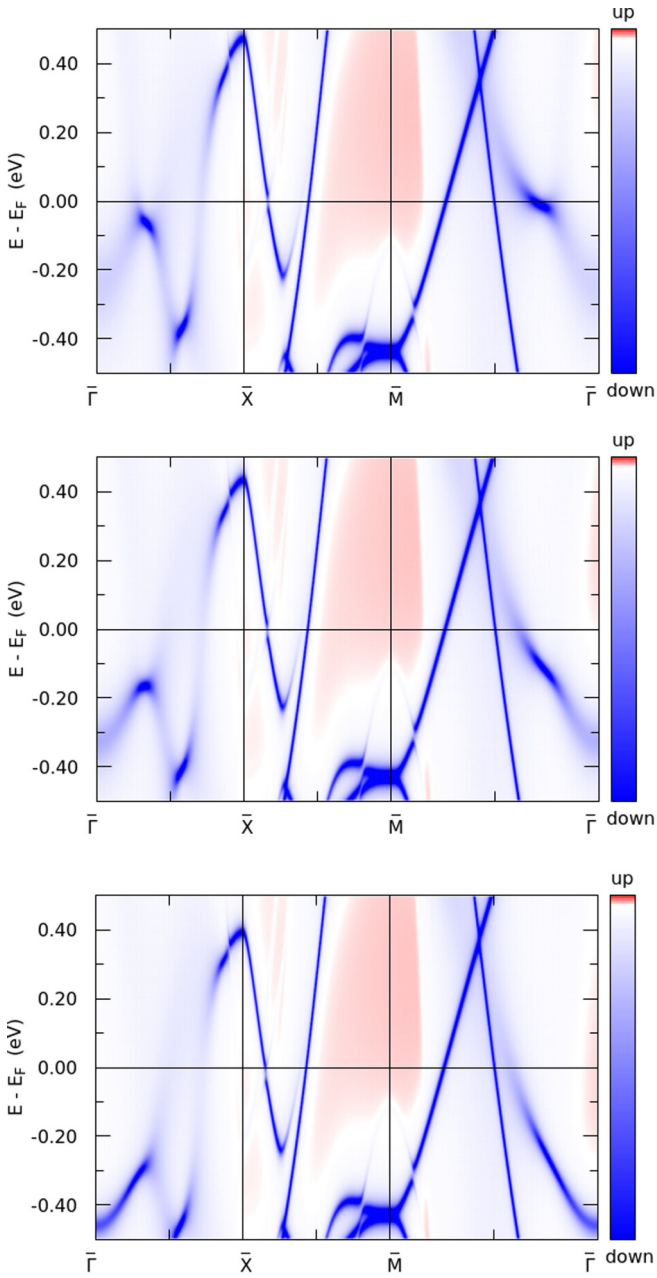

FIG. 8. Fe-projected Bloch spectral function for a Fe monolayer on Cu(001), color coded to indicate the predominantly down-spin polarization of electronic states at the Fermi level. From top to bottom: Results for $E_{field} = -5.2$, 0, or +5.2 (V/nm).

line with full circles in Fig. 11 with Fig. 7). On the other hand, the magnetic moments decrease almost linearly with increasing E_{field} for the subsurface Fe_1 layer (blue line with empty circles in Fig. 11). The total change of the magnetic moment across the investigated range of E_{field} is about 0.5% for both layers, similarly as in the case of a Fe monolayer on Cu(001).

The adiabatic magnon dispersion is shown in Fig. 12. Some qualitative differences appear with respect to the case of a Fe bilayer suspended in vacuum. In particular, the substrate removes the energy degeneracy also for $\boldsymbol{q}$ points along the $\overline{X}$–$\overline{M}$ path. On the other hand, the suspended bilayer and

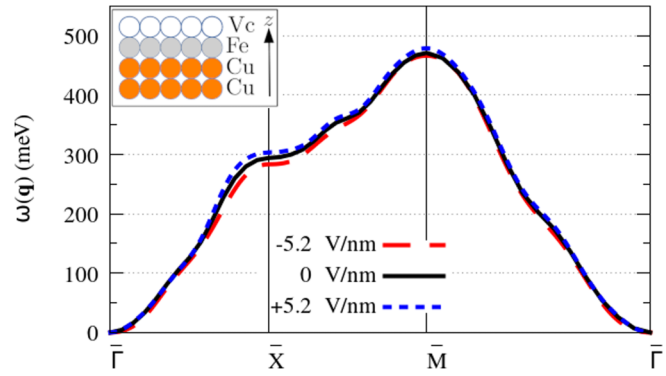

FIG. 9. Adiabatic magnon spectrum of a Fe monolayer on Cu(001) for selected values of $E_{field} = -5.2$, 0, and +5.2 (V/nm).

the bilayer deposited on Cu(001) exhibit alike involvement of individual iron sheets' moments in hosting the magnons. The two eigenmodes involve precession of magnetic moments equally from both iron sheets near to $\overline{\Gamma}$, and from only one or the other layer away from the origin of the Brillouin zone. The high-energy branch involves only the subsurface Fe_1 atoms along the $\overline{X}$–$\overline{M}$ path, whereas the low-energy branch involves only the surface Fe_2 atoms. A similar $\boldsymbol{q}$-resolved decomposition can be observed for the suspended bilayer of Fig. 4.

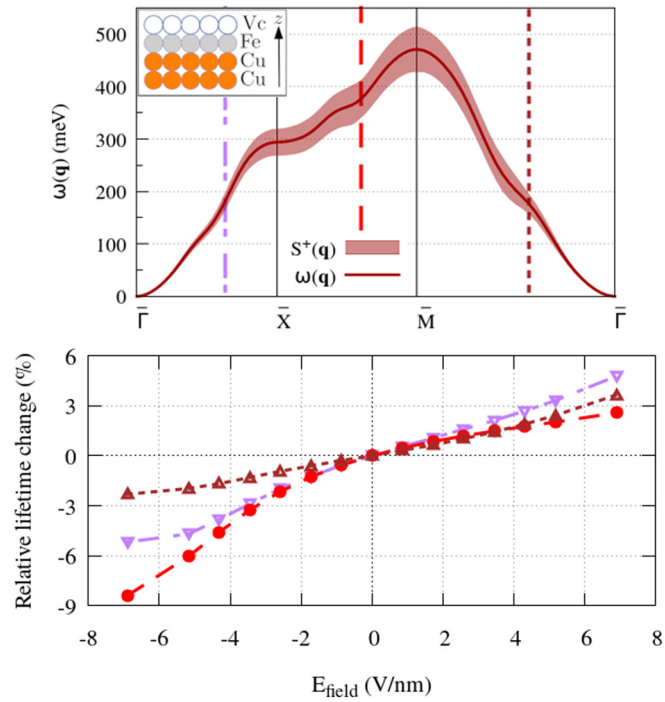

FIG. 10. Top panel: Magnon spectrum for a Fe monolayer on Cu(001) for $E_{field} = 0$, depicting eigenvalues according to Eq. (2) (darker line) together with the corresponding intensity of Stoner excitations obtained by evaluating Eq. (7) (lighter shaded area, in arbitrary units). Bottom panel: Relative change of the magnon lifetime (obtained as the inverse of the Stoner intensity) with E_{field}, for three choices of the $\boldsymbol{q}$-vector indicated in the top graph by differently dashed vertical lines of matching colors.

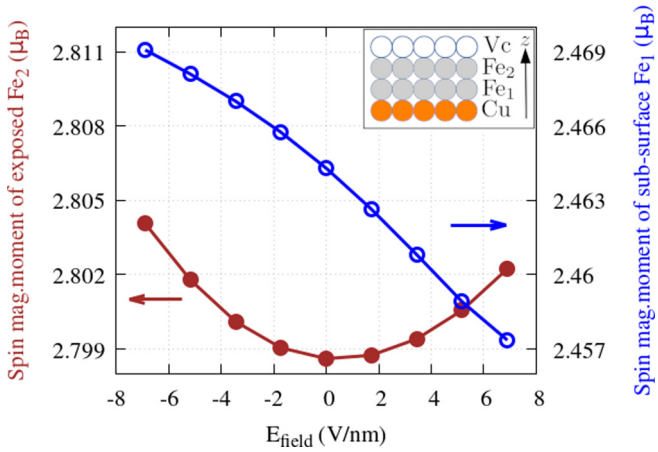

FIG. 11. Spin magnetic moment versus E_{field} for the exposed Fe_2 (brown full circles, left scale) and subsurface Fe_1 (blue empty circles, right scale) for an iron bilayer over Cu(001) substrate.

We then evaluate again the gap $\Delta E = \omega_2(\overline{\Gamma}) - \omega_1(\overline{\Gamma})$ between the high- and low-energy magnon branches as a function of E_{field}. For the suspended bilayer, its influence was symmetric with respect to the polarity and quite small (Fig. 5). The presence of the substrate changes the situation dramatically, as can be seen in Fig. 13: the total variation of ΔE is now about 30% (in contrast with 0.05% for the case of a bilayer suspended in vacuum, see Sec. III A) and it is asymmetric with respect to E_{field}. This outcome is not only due to the different effect of the perturbation on the magnetic moments for Fe_1 and Fe_2 atoms (see Fig. 11) but it is also due to the E_{field}-induced modifications of the interlayer Heisenberg exchange couplings [61]. As discussed, e.g., in Ref. [65], these interactions are responsible for an additional indirect contribution to the Fe-Fe exchange interactions, which is mediated by Cu atoms. This can be seen in Fig. 14 where we present the interlayer coupling constants J_{IJ}^{12} for different values of the external electric field. The largest variation occurs among the nearest neighbors and then decays rapidly with the distance $|\boldsymbol{R}_I - \boldsymbol{R}_J|$.

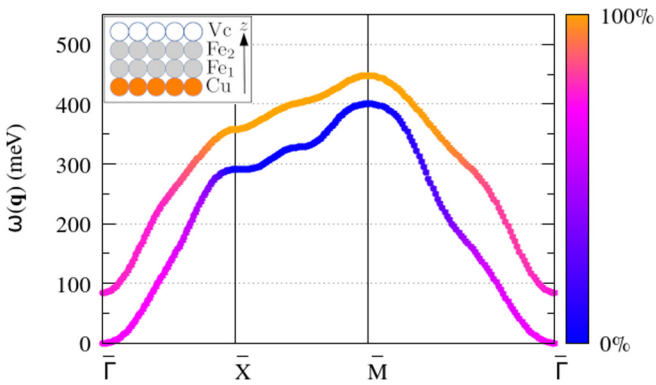

FIG. 12. Adiabatic magnon spectrum for a Fe bilayer on Cu(001) and with $E_{field} = 0$. The color coding represents the magnitude of the corresponding complex eigenvectors, projected on the Fe_2 layer (as in Fig. 4).

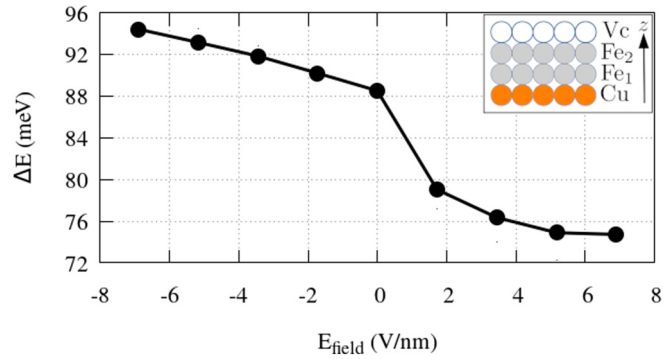

FIG. 13. Energy gap between the high- and low-energy magnon branches at $\boldsymbol{q} = \overline{\Gamma}$ for an iron bilayer on Cu(001) (cf. Fig. 12) evaluated as a function of E_{field}.

IV. DISCUSSION

The calculations presented in Sec. III reveal that certain features of magnon spectra can be controlled by an applied electric field, besides aspects already considered in the literature as a consequence of voltage-controlled magnetocrystalline anisotropy in 2D thin films [60,66,67], multiferroic coupling [12,13], induced effective DMI [14–19], or strain from a piezoelectric substrate [68]. In particular, we see that a finite E_{field} perturbation may lead to sizable changes in the magnon lifetime, even in a case for which the adiabatic dispersion $\omega(\boldsymbol{q})$ is fairly unaffected (compare Fig. 9 with Fig. 10). The stability of this latter quantity can be linked to the balance between the tiny asymmetric increase of the spin magnetic moment for $|E_{field}| > 0$ on the one hand (Fig. 7), and the strengthening of Heisenberg J_{ij} parameters (by few tenths of meV) for nearest-neighbor Fe atoms on the other hand.

The robustness of $\omega(\boldsymbol{q})$ against E_{field} suggests that the main reason why the magnon lifetime changes with E_{field} is that the Bloch spectral functions entering Eq. (7) are significantly modified by the electric field. A negative E_{field} couples mainly with minority electronic states, just below the Fermi level (Fig. 8, top). This results in more minority states appearing closer to the Fermi level, with a shift of the $n_{Fe}^{\downarrow}(E)$ bump

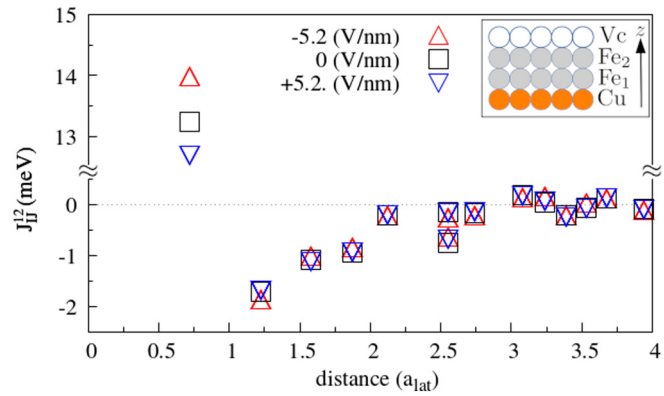

FIG. 14. Inter-layer Heisenberg exchange couplings J_{IJ}^{12} for a Fe bilayer on Cu(001) plotted as a function of the $|\boldsymbol{R}_I - \boldsymbol{R}_J|$ distance, for $E_{field} = -5.2$, 0, and +5.2 (V/nm).

toward higher energy from its original position at around $E = -250$ meV (Fig. 6). The net result is an increase in Stoner intensity, which is shown in Fig. 10 (bottom) as a noteworthy enhancement of Landau damping at every depicted $\boldsymbol{q}$-point. An opposite shift of the electronic spectral weight, i.e., to lower energies, takes place for $\mathrm{E_{field}} > 0$. This results in longer magnon lifetimes due to the repulsion to deeper energies of the same minority electronic states discussed above, until they are pushed below the $[E_{\min}, E_{\max}]$ energy interval sampled by Eq. (7), and progressively allow only fewer competing Stoner excitations.

For both electric field polarities, saturation of the change in Landau damping appears when the perturbation no longer can redistribute spin-polarized spectral weight within the energy interval spanned by the magnon.

The scenario of a Fe bilayer on Cu(001) shows $\mathrm{E_{field}}$-induced changes in the magnon dispersion relations even before considering finite lifetime effects. Interestingly, the dependence of the magnetic moments on $\mathrm{E_{field}}$ exhibits different trends for each of the two iron sheets (see Fig. 11). In both cases, the magnetic moment is larger than in bulk bcc Fe, as it is common for surfaces. This is a consequence of the thin film straining to follow the different lattice parameters of the substrate. In addition, the reduced dimensionality, or more specifically, the reduced number of Fe atoms with alike neighbours also plays a role. However, whereas the surface $\mathrm{Fe_2}$ layer shows an approximately parabolic and slightly asymmetric variation of the spin magnetic moment with $\mathrm{E_{field}}$, similar to the case of a monolayer (cf. Fig. 7), the subsurface $\mathrm{Fe_1}$ layer contiguous to copper shows a monotonous quasilinear dependence instead. It seems that exposition to the electric field perturbation with or without an in-between layer that can provide metallic screening is more important than the proximity to the nonmagnetic substrate in governing these trends.

After the nonmagnetic Cu(001) substrate has lifted the degeneracy between the two iron sheets, our calculations show in Fig. 11 different trends for the magnetic moment dependence on $\mathrm{E_{field}}$ from subsurface $\mathrm{Fe_1}$ contiguous to copper and from exposed $\mathrm{Fe_2}$ facing vacuum. The change spans an alike interval of about 0.012 μ_B. The deeper iron sheet shows an approximately parabolic and slightly asymmetric variation in the spin magnetic moment, similar to the monolayer case of Fig. 7. The variation is linear instead for the surface $\mathrm{Fe_2}$ atoms.

For all cases under consideration, we find a $\omega_1(\boldsymbol{q})$ solution to Eq. (2) that requires zero energy at the $\overline{\Gamma}$ point, i.e., a Goldstone mode. The second eigenmode $\omega_2(\boldsymbol{q})$, when present, starts from the origin of the Brillouin zone in a similar quadratic fashion, which is a consequence of the ferromagnetic ground-state order. While small-wavelength magnons are equally hosted by both layers, in the presence of a copper substrate the two modes are neither degenerate in energy nor in the way that they involve Fe atoms from one or the other sheet at large $\boldsymbol{q}$.

Upon including a finite electric field, the Goldstone theorem continues to apply and the lower-energy $|\omega_1(\boldsymbol{q})\rangle$ branch continues to start from zero energy. The ΔE gap at $\overline{\Gamma}$ strongly depends on the presence of the nonmagnetic substrate (cf. Fig. 5 versus Fig. 13). In this case the applied perturbation significantly modifies the higher-energy $\omega_2(\boldsymbol{q} = \overline{\Gamma})$ solution by changing both the interlayer Heisenberg exchange parameters J_{IJ}^{12}, and layer-resolved magnetic moment m_1^z, m_2^z that enter Eq. (10). The resulting energy difference gets wider for negative $\mathrm{E_{field}}$, and shrinks but remains open when inverting the sign of the perturbation. A negative electric field not only increases the spin magnetic moment of both $\mathrm{Fe_1}$ and $\mathrm{Fe_2}$ atoms which are equally involved in the $\omega_n(\boldsymbol{q} \to \overline{\Gamma})$ limit, but it also strengthens the J_{ij}^{12} interlayer interaction (Fig. 14). The opposite happens for $\mathrm{E_{field}} > 0$.

In summary, the electric field perturbation acts across the dielectric barrier of Fig. 1 by modulating the influence of the nonmagnetic substrate. This mechanism provides different Landau damping even for limited changes in the purely adiabatic dispersion relation of magnons in simple metallic thin films. The same mechanism also offers possible routes to engineer specific changes in the magnon spectrum of more complex, thicker 2D systems, such as the energy gap at the $\overline{\Gamma}$ point.

We have focused here for clarity on simple examples with a thin ferromagnetic film. However, the interplay between metallic screening and the $\mathrm{E_{field}}$-controlled variation of the hybridization across magnetic/nonmagnetic layers can be expected to become more complex for thicker systems, where the penetration depth of the perturbation is gradually reduced. Similarly, preliminary calculations show how the case of colinear antiferromagnetic order can also be affected, when the $\mathrm{E_{field}}$ alters the net compensation between antiparallel magnetic moments, or through other mechanisms already considered in the literature [69,70]. Other works have also examined the impact on DMI [60,71] and skyrmion lattices in particular [72], rare earths [73], or cases where the applied electric field is spatially inhomogeneous [74,75].

V. CONCLUSIONS

Magnon spectra of magnetic/nonmagnetic metallic heterostructures can be manipulated by external gating electric field. Our *ab initio* calculations for test systems of a Fe monolayer and Fe bilayer, both suspended in vacuum and deposited on Cu(001), demonstrate that this perturbation can induce sizable modifications in finite magnon lifetimes from Landau damping, besides possible changes in the purely adiabatic dispersion relations already considered in the literature. The changes in magnon lifetimes can be related to modifications of the electronic structure, in particular, in the layer-resolved spin-polarized Bloch spectral functions.

For systems with more magnon dispersion branches, variation of the gap between high- and low-energy eigenmodes with the external field $\mathrm{E_{field}}$ can be expected. As the $\mathrm{E_{field}}$ perturbation controls the degree of hybridization among magnetic/nonmagnetic layers, one can expect considerable variability in how the magnon spectra are affected by the external field, depending on the choice of the substrate and the thickness of the magnetic film.

ACKNOWLEDGMENTS

We gratefully acknowledge computational resources from the Information Technology for Innovation (IT4I) Grants

No. OPEN-19-45 and No. OPEN-22-40 (Czech National Computing Centre, Ostrava, Czech Republic). Part of this work was supported by the Deutsche Forschungsgemeinschaft via Grant No. DFG EB 154/35, by the Czech Science Foundation via Grant EXPRO No. 19-28375X, and by the Czech Minisitry of Education, Youth and Sports via Grant No. CEDAMNF CZ.02.1.01/0.0/0.0/15_003/0000358 (Computational and Experimental Design of Advanced Materials with New Functionalities). We thank L. Sandratskii for formative discussions and insight.

[1] S. O. Demokritov and A. N. Slavin, *Magnonics*, Topics in Applied Physics, Vol. 125, edited by S. O. Demokritov and A. N. Slavin (Springer-Verlag, Berlin, 2013)
[2] A. Chumak, V. Vasyuchka, A. Serga, and B. Hillebrands, Nat. Phys. **11**, 453 (2015).
[3] C. Tannous and J. Gieraltowski, J. Mater. Sci. Mater. Electron. **26**, 4675 (2015).
[4] K. Zakeri, Phys. C **549**, 164 (2018).
[5] A. Mahmoud, F. Ciubotaru, F. Vanderveken, A. V. Chumak, S. Hamdioui, C. Adelmann, and S. Cotofana, J. Appl. Phys. **128**, 161101 (2020).
[6] J. Xu, L. Jin, Z. Liao, Q. Wang, X. Tang, Z. Zhong, and H. Zhang, Front. Mater. **7**, 594386 (2020).
[7] M. P. Kostylev, A. A. Serga, T. Schneider, B. Leven, and B. Hillebrands, Appl. Phys. Lett. **87**, 153501 (2005).
[8] C. Y. Guo, C. H. Wan, X. Wang, C. Fang, P. Tang, W. J. Kong, M. K. Zhao, L. N. Jiang, B. S. Tao, G. Q. Yu, and X. F. Han, Phys. Rev. B **98**, 134426 (2018).
[9] Q. Wang, M. Kewenig, M. Schneider, R. Verba, F. Kohl, B. Heinz, M. Geilen, M. Mohseni, B. Lägel, F. Ciubotaru, C. Adelmann, C. Dubs, S. D. Cotofana, O. V. Dobrovolskiy, T. Brächer, P. Pirro, and A. V. Chumak, Nat. Electron. **3**, 765 (2020).
[10] G. T. Rado, C. Vittoria, J. M. Ferrari, and J. P. Remeika, J. Appl. Phys. **50**, 2036 (1979).
[11] T. Liu, Spin-wave spintronics, Ph.D. thesis, University of Missouri, 2013.
[12] P. Rovillain, R. De Sousa, Y. Gallais, A. Sacuto, M. A. Méasson, D. Colson, A. Forget, M. Bibes, A. Barthélémy, and M. Cazayous, Nat. Mater. **9**, 975 (2010).
[13] V. Risinggård, I. Kulagina, and J. Linder, Sci. Rep. **6**, 1 (2016).
[14] T. Liu and G. Vignale, Phys. Rev. Lett. **106**, 247203 (2011).
[15] X. Zhang, T. Liu, M. E. Flatté, and H. X. Tang, Phys. Rev. Lett. **113**, 037202 (2014).
[16] V. N. Krivoruchko, A. S. Savchenko, and V. V. Kruglyak, Phys. Rev. B **98**, 024427 (2018).
[17] B. Rana and Y. C. Otani, Commun. Phys. **2**, 90 (2019).
[18] A. S. Savchenko and V. N. Krivoruchko, J. Magn. Magn. Mater. **474**, 9 (2019).
[19] V. N. Krivoruchko, Low Temp. Phys. **46**, 820 (2020).
[20] C. Etz, L. Bergqvist, A. Bergman, A. Taroni, and O. Eriksson, J. Phys.: Condens. Matter **27**, 243202 (2015).
[21] S. Zhang, R. Xu, N. Luo, and X. Zou, Nanoscale **13**, 1398 (2021).
[22] P. Dean, Rev. Mod. Phys. **44**, 127 (1972).
[23] P. Buczek, S. Thomas, A. Marmodoro, N. Buczek, X. Zubizarreta, M. Hoffmann, T. Balashov, W. Wulfhekel, K. Zakeri, and A. Ernst, J. Phys.: Condens. Matter **30**, 423001 (2018).
[24] A. Azevedo, A. B. Oliveira, F. M. de Aguiar, and S. M. Rezende, Phys. Rev. B **62**, 5331 (2000).
[25] P. Landeros, R. E. Arias, and D. L. Mills, Phys. Rev. B **77**, 214405 (2008).
[26] X. Xue, G. Dong, Z. Zhou, D. Xian, Z. Hu, W. Ren, Z. G. Ye, W. Chen, Z. D. Jiang, and M. Liu, ACS Appl. Mater. Interfaces **9**, 43188 (2017).
[27] A. T. Costa, R. B. Muniz, and D. L. Mills, Phys. Rev. B **68**, 224435 (2003).
[28] S. V. Halilov, H. Eschrig, A. Y. Perlov, and P. M. Oppeneer, Phys. Rev. B **58**, 293 (1998).
[29] A. Liechtenstein, M. Katsnelson, and V. Gubanov, J. Phys. F: Met. Phys. **14**, L125 (1984).
[30] A. Liechtenstein, M. Katsnelson, V. Antropov, and V. Gubanov, J. Magn. Magn. Mater. **67**, 65 (1987).
[31] L. Udvardi, L. Szunyogh, K. Palotás, and P. Weinberger, Phys. Rev. B **68**, 104436 (2003).
[32] S. Mankovsky and H. Ebert, Phys. Rev. B **96**, 104416 (2017).
[33] J. Kuneš and V. Kamberský, Phys. Rev. B **65**, 212411 (2002).
[34] M. C. Hickey and J. S. Moodera, Phys. Rev. Lett. **102**, 137601 (2009).
[35] P. He, X. Ma, J. W. Zhang, H. B. Zhao, G. Lüpke, Z. Shi, and S. M. Zhou, Phys. Rev. Lett. **110**, 077203 (2013).
[36] M. Pajda, J. Kudrnovský, I. Turek, V. Drchal, and P. Bruno, Phys. Rev. B **64**, 174402 (2001).
[37] J. Rusz, I. Turek, and M. Diviš, Phys. B: Condens. Matter **378–380**, 1079 (2006).
[38] A. Jacobsson, B. Sanyal, M. Ležaić, and S. Blügel, Phys. Rev. B **88**, 134427 (2013).
[39] L. Bergqvist, A. Taroni, A. Bergman, C. Etz, and O. Eriksson, Phys. Rev. B **87**, 144401 (2013).
[40] K. Yosida, *Theory of Magnetism* (Springer-Verlag, Berlin, Heidelberg, New York, 1996).
[41] J. Kübler, Acta Phys. Pol. A, **97**, 165 (2000).
[42] Y. Kakehashi, *Modern Theory of Magnetism in Metals and Alloys* (Springer, Berlin, Heidelberg, 2012).
[43] M. I. Katsnelson and A. I. Lichtenstein, J. Phys.: Condens. Matter **16**, 7439 (2004).
[44] P. Buczek, A. Ernst, and L. M. Sandratskii, Phys. Rev. B **84**, 174418 (2011).
[45] J. B. Staunton, J. Poulter, and B. Ginatempo, Phys. Rev. B **62**, 1075 (2000).
[46] R. Kubo, J. Phys. Soc. Jpn. **12**, 570 (1957).
[47] V. Antropov, J. Magn. Magn. Mater. **262**, L192 (2003).
[48] J. Kirschner and S. Suga, Surf. Sci. **178**, 327 (1986).
[49] D. Venus and J. Kirschner, Phys. Rev. B **37**, 2199 (1988).
[50] R. Vollmer, M. Etzkorn, P. S. Anil Kumar, H. Ibach, and J. Kirschner, Phys. Rev. Lett. **91**, 147201 (2003).
[51] H. Ebert, D. Ködderitzsch, and J. Minár, Rep. Prog. Phys. **74**, 096501 (2011).
[52] D. M. Edwards and M. A. Rahman, J. Phys. F: Met. Phys. **8**, 1501 (1978).

[53] M. M. Odashima, A. Marmodoro, P. Buczek, A. Ernst, and L. Sandratskii, Phys. Rev. B **87**, 174420 (2013).
[54] H. Ebert, The Munich SPR-KKR package.
[55] S. H. Vosko, L. Wilk, and M. Nusair, Can. J. Phys. **58**, 1200 (1980).
[56] R. Zeller, P. H. Dederichs, B. Újfalussy, L. Szunyogh, and P. Weinberger, Phys. Rev. B **52**, 8807 (1995).
[57] See Supplemental Material at http://link.aps.org/supplemental/10.1103/PhysRevB.105.174411 for results calculated also with relaxed vertical spacing between the layers, which lead to similar conclusions.
[58] R. Allenspach and A. Bischof, Phys. Rev. Lett. **69**, 3385 (1992).
[59] C. A. Vaz, J. A. Bland, and G. Lauhoff, Rep. Prog. Phys. **71**, 056501 (2008).
[60] E. Simon, A. Marmodoro, S. Mankovsky, and H. Ebert, Phys. Rev. B **103**, 064406 (2021).
[61] S. Mankovsky, E. Simon, S. Polesya, A. Marmodoro, and H. Ebert, Phys. Rev. B **104**, 174443 (2021).
[62] H. Zhang, M. Richter, K. Koepernik, I. Opahle, F. Tasnádi, and H. Eschrig, New J. Phys. **11**, 043007 (2009).
[63] P. A. Ignatiev and V. S. Stepanyuk, Phys. Rev. B **84**, 075421 (2011).
[64] R. B. Muniz and D. L. Mills, Phys. Rev. B **66**, 174417 (2002).
[65] S. Polesya, S. Mankovsky, O. Sipr, W. Meindl, C. Strunk, and H. Ebert, Phys. Rev. B **82**, 214409 (2010).
[66] T. Kawabe, K. Yoshikawa, M. Tsujikawa, T. Tsukahara, K. Nawaoka, Y. Kotani, K. Toyoki, M. Goto, M. Suzuki, T. Nakamura, M. Shirai, Y. Suzuki, and S. Miwa, Phys. Rev. B **96**, 220412(R) (2017).
[67] S. Miwa, M. Suzuki, M. Tsujikawa, T. Nozaki, T. Nakamura, M. Shirai, S. Yuasa, and Y. Suzuki, J. Phys. D. Appl. Phys. **52**, 063001 (2018).
[68] H. Qin, R. Dreyer, G. Woltersdorf, T. Taniyama, and S. van Dijken, Adv. Mater. **33**, 2100646 (2021).
[69] R. Cheng, M. W. Daniels, J. G. Zhu, and D. Xiao, Sci. Rep. **6**, 24223 (2016).
[70] X.-G. Wang, G.-H. Guo, and J. Berakdar, Appl. Phys. Lett. **117**, 242406 (2020).
[71] T. H. Kim, P. Grünberg, S. H. Han, and B. K. Cho, Phys. Rev. B **97**, 184427 (2018).
[72] H. B. Chen and Y. Q. Li, Appl. Phys. Express **12**, 093003 (2019).
[73] A. O. Leon, A. B. Cahaya, and G. E. W. Bauer, Phys. Rev. Lett. **120**, 027201 (2018).
[74] V. Krivoruchko and A. Savchenko, Proc. 2019 IEEE 9th Int. Conf. Nanomater. Appl. Prop. N. 2019, 9 (2019).
[75] V. Krivoruchko and A. Savchenko, Proc. 2019 IEEE 9th Int. Conf. Nanomater. Appl. Prop. N. 2019, 1 (2019).